

# Plasmonic Nanogap-Enhanced Raman Scattering Using a Resonant Nanodome Array

Hsin-Yu Wu, Charles J. Choi, and Brian T. Cunningham\*

*The optical properties and surface-enhanced Raman scattering (SERS) of plasmonic nanodome array (PNA) substrates in air and aqueous solution are investigated. PNA substrates are inexpensively and uniformly fabricated with a hot spot density of  $6.25 \times 10^6 \text{ mm}^{-2}$  using a large-area nanoreplica moulding technique on a flexible plastic substrate. Both experimental measurement and numerical simulation results show that PNAs exhibit a radiative localized surface plasmon resonance (LSPR) due to dipolar coupling between neighboring nanodomains and a non-radiative surface plasmon resonance (SPR) resulting from the periodic array structure. The high spatial localization of electromagnetic field within the  $\sim 10 \text{ nm}$  nanogap together with the spectral alignment between the LSPR and excited and scattered light results in a reliable and reproducible spatially averaged SERS enhancement factor (EF) of  $8.51 \times 10^7$  for Au-coated PNAs. The SERS enhancement is sufficient for a wide variety of biological and chemical sensing applications, including detection of common metabolites at physiologically relevant concentrations.*

## 1. Introduction

Metallic nanostructures exhibit their remarkable and unique optical properties due to the excitation of either surface plasmon-polariton (SPP) or localized surface plasmon-polariton (LSP) modes. In the past decade, these phenomena have been used for a wide range of applications in biological and chemical detection such as metal-enhanced fluorescence,<sup>[1,2]</sup> label-free surface plasmon resonance (SPR) or LSP resonance (LSPR) sensing,<sup>[3,4]</sup> and surface-enhanced Raman scattering (SERS).<sup>[5,6]</sup> These phenomena have been applied to devices that include plasmonic tweezers,<sup>[7,8]</sup> lasers,<sup>[9,10]</sup> and solar cells.<sup>[11,12]</sup> Among these applications, SERS spectroscopy

is a powerful and versatile tool for both qualitative and quantitative analysis of chemical constituents and structure by increasing the Raman scattering cross-sections of analytes residing in close proximity to a metallic nanostructure that supports highly concentrated electromagnetic (EM) fields associated with LSPR at EM hot spots. It has been shown that SERS spectroscopy has opened the way to a simple yet effective approach for chemical and biological sensing and identification,<sup>[13,14]</sup> extending to the potential for selective detection of single molecules.<sup>[15,16]</sup>

There are many approaches reported in the literature for producing SERS-active surfaces, which can be broadly categorized into two groups: randomly roughened surfaces<sup>[17–23]</sup> and ordered nanoparticle arrays.<sup>[24–36]</sup> Randomly roughened surfaces (this group may also include individual nanoparticles) typically exhibit localized positions of high enhancement arising at sharp corners or at junctions of randomly formed protrusions. This enhancement can be further enhanced when two metallic nanoobjects are brought very close to each other. The LSP modes of each nanoobject then interact with each other and form hybridized or gap surface plasmon-polariton (SPP) modes, particularly suitable for single-molecule detection.<sup>[15,16]</sup> However, due to the intrinsic large variation of enhancement and the difficulty of predicting the optical

H.-Y. Wu, C. J. Choi, Prof. B. T. Cunningham  
Department of Electrical and Computer Engineering  
University of Illinois at Urbana-Champaign  
208 North Wright Street, Urbana, IL 61801, USA  
E-mail: bcunning@illinois.edu

Prof. B. T. Cunningham  
Department of Bioengineering  
University of Illinois at Urbana-Champaign  
1304 West Springfield Avenue, Urbana, Illinois 61801, USA



DOI: 10.1002/sml.201200712

response of such random structures, this approach is not suitable for reproducible SERS measurements with a well-characterized enhancement factor (EF). On the other hand, due to the ability to accurately design and model/engineer structures with nanometer scale precision, nanoparticle arrays enable us to select geometric variables (e.g., size, shape and period) and to tailor the optical properties of a structure for boosting the SERS EF in a predictable way. Typically, such ordered arrays can provide a high EF that is uniform and reproducible for applications that require quantitation of analyte concentration. However, the majority of such approaches are not commercially feasible for single-use disposable detection applications due to multistep nanofabrication processes and/or low throughput and costly patterning approaches (such as electron beam lithography or focused ion beam milling). For SERS to find widespread applications in routine chemical analysis, manufacturing process control, point-of-care diagnostics, and pharmaceutical research, the SERS device structure must be inexpensively manufacturable over large surface areas while providing a robust EF.

In this paper, we experimentally and numerically demonstrate that spectral LSP properties of plasmonic nanodome array (PNA) substrates fabricated using a low-cost, large-area nanoreplica molding processes can be tailored toward maximizing SERS EF by controlling the thickness of a single  $\text{SiO}_2$  thin film layer. We observe a small blueshift of the LSPR wavelength and no change in SPR wavelength as we decrease the dome-to-dome gap spacing. When inter-dome spacing is reduced to  $\sim 10$  nm, the intense EM intensities associated with LSPR spatially concentrated within the nanogaps form EM hot spots with a density of  $6.25 \times 10^6 \text{ mm}^{-2}$ . Measured SERS spectra show that Au-PNA substrates with 10-nm gap spacing exhibits a reliable spatially averaged SERS EF of  $8.51 \times 10^7$ . We compare the performance of Ag-PNA substrates, Au-PNA substrates, and a commercially available SERS substrate. In this study, we perform electromagnetic computer simulations to determine how the PNA dimensional parameters affect the near-field and far-field characteristics, demonstrating excellent agreement with experimentally measured characteristics. Detection of urea in solution is used to demonstrate the clinical potential for in-line, real-time monitoring of urinary metabolite concentration.

## 2. Results and Discussion

### 2.1. Optical Characterization of Ag-PNA

**Figure 1(a)** shows a schematic cross section of a two-dimensional Ag-PNA structure comprised of an Ag film, a  $\text{SiO}_2$  film, and a replica-molded UV curable polymer (UVCP) layer

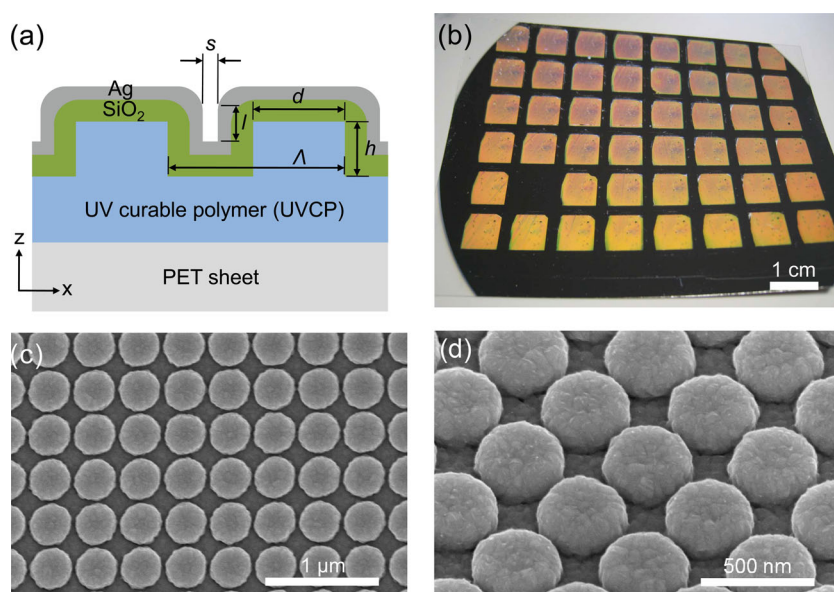


**Figure 1.** (a) Schematic cross-sectional illustration of two Ag-PNA unit cells. (b) Image of the completed nanodome array substrate fabricated on a flexible PET sheet. (c) and (d) SEM images of the Ag-PNA surface.

fabricated upon a flexible polyethylene terephthalate (PET) substrate. In order to produce PNA substrates with a process that is amenable to manufacturing scale-up, we used a large-area nanoreplica molding process to fabricate a two-dimensional square lattice of cylinders with a period ( $\Lambda$ ) of 400 nm, a diameter ( $d$ ) of 250 nm, and a height ( $h$ ) of 130 nm using a low refractive index (RI) UVCP (Gelest Inc.) layer over an area of  $150 \times 100 \text{ mm}^2$ .<sup>[33]</sup> Figure 1(b) shows a photograph of an Ag-PNA on a flexible PET substrate, over a  $75 \times 100 \text{ mm}^2$  surface area. Each Ag-PNA die (orange colored in the photo) is  $8 \times 8 \text{ mm}^2$  with a density of  $6.25 \times 10^6 \text{ mm}^{-2}$  hot spots, which are located between adjacent nanodomains. Figure 1(c) and (d) show scanning electron microscopy (SEM) images of the resulting Ag-PNA with square lattice symmetry.

To excite the LSPR of metallic nanoparticles, it is necessary to provide an electric field component normal to the metal-dielectric interface, resulting in an LSPR excitation condition that is strongly polarization-dependent.<sup>[37]</sup> For the case of two “isolated” adjoining nanoparticles or dimer structures illuminated by light polarized parallel to the interparticle axis, the induced charges accumulating on the opposite sides of the inter-particle gap attract each other, resulting in a reduced restoring force inside each nanoparticle when compared with that inside a single nanoparticle and thus in a longer LSPR wavelength ( $\lambda_{\text{LSPR}}$ ). Likewise, incident light that is polarized perpendicular to the interparticle axis results in accumulation of charge with identical polarity on opposite sides of the gap, which repel each other, and thus result in a decrease in  $\lambda_{\text{LSPR}}$ . The inter-particle plasmon coupling causes a remarkable redshift in the spectral position of the LSPR extinction maximum with decreasing gap spacing for the parallel polarization and a less pronounced blueshift for the perpendicular polarization.<sup>[38]</sup> However, in the PNA structure, in which neighboring nanodomains are connected with a continuous 200-nm-thick metal film, the region within the

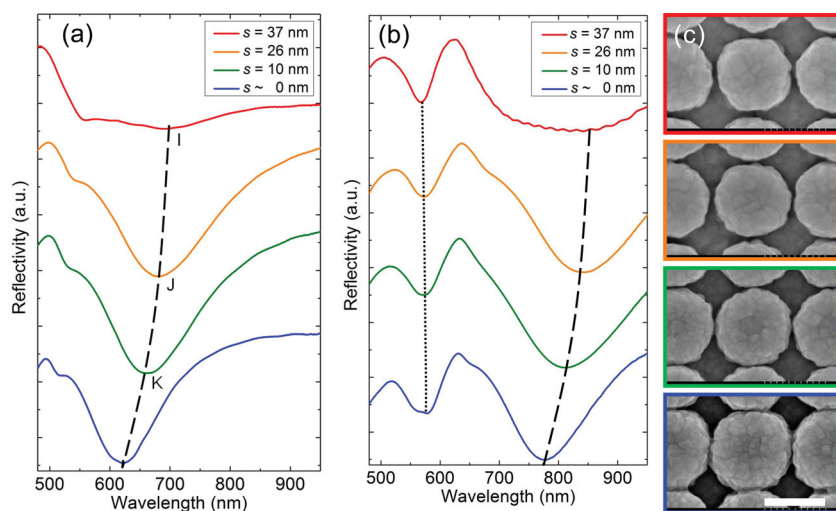


**Figure 2.** Measured far-field reflection spectra of Ag-PNA substrates with four different inter-dome separation distances for air (a) and water (b) as the covering media. The labeling of I, J and K indicates the spectral position of the LSPR for the calculation of their respective effective cavity lengths. (c) The corresponding SEM close-up views of the gap regions near the inter-dome spacing. The scale bar in (c) represents 300 nm. See Supporting Information Figure S1 for further details.

dome-to-dome gap spacing can be considered to act as a vertical plasmonic nanocavity,<sup>[39]</sup> and therefore the spectral position of LSPR associated with the geometrical dimensions of such a nanocavity is mainly determined by inter-dome separation distance ( $s$ ) and cavity length ( $l$ ), shown in Figure 1(a), as well as the material parameters of the metal and the dielectric environment.

**Figure 2** shows experimental reflection spectra measured with air (Figure 2a) and water (Figure 2b) media covering an Ag-PNA surface for four different inter-dome separation distances ( $s = 37, 26, 10$ , and  $\sim 0$  nm). Their SEM images are correspondingly shown in Figure 2(c). Because Ag-PNA substrates coated with a fixed 200-nm-thick silver film are not transparent in the visible regime, LSPR extinction spectra are measured in reflectance mode and reflectance minimum wavelength ( $\lambda_{\min}$ ) corresponds to LSPR extinction maximum wavelength ( $\lambda_{\text{LSPR}}$ ). For plasmon resonances at  $\lambda_{\text{LSPR}}$  marked by I, J and K in Figure 2(a), the resonant coupling efficiency increases with decreasing inter-dome spacing ( $s$ ) due to stronger plasmon coupling between dipolar moments of neighboring nanodomains. Further decreasing inter-dome spacing causes weaker plasmon coupling and hence low resonant coupling efficiency as domes slightly touch each other ( $s \sim 0$  nm), shown in the blue curve of Figure 2(a). The result of the redshift in  $\lambda_{\text{LSPR}}$  arising from the refractive index (RI) change of the background media from air ( $n = 1$ ) to water ( $n \sim 1.33$ ) is presented in the dashed curve of Figure 2(b). We also observe a distinct blueshift in  $\lambda_{\text{LSPR}}$  as inter-dome spacing is decreased from 37 to 0 nm as controlled by increasing the thickness of the  $\text{SiO}_2$  layer. The increasing  $\text{SiO}_2$  thickness reduces the effective volume of the nanocavity within the inter-dome space region, which in turn results in the observed blueshift, as shown in the respective dashed curves of Figure 2(a) and (b). See Supporting Information Figure S1 for further details.

To explore the relationship between observed blueshifted  $\lambda_{\text{LSPR}}$  and the geometrical dimensions of the effective volume within the inter-dome space region, the optical responses of Ag-PNA structures were simulated using the finite difference time domain (FDTD) method. The SEM image shown in Figure 1(d) and the AFM images shown in Supporting Information Figure S2 indicate that the profile the nanodome structure is a cylinder with a flat top surface as shown in Figure 1(a). The hot-spot region is located within the nanocavity defined by the cavity length ( $l$ ) and the inter-dome spacing ( $s$ ). In order to simplify FDTD 3D modeling, the shape of nanodome was approximately modeled as a periodic cylinder dimer structure composed of Ag,  $\text{SiO}_2$  and UVCP with two variables: gap spacing,  $s$  and effective cavity length,  $l_{\text{eff}}$ , as shown in the inset in **Figure 3**. Figure 3 shows simulated LSPR wavelength ( $\lambda_{\text{LSPR}}$ ) as a function of effective cavity length ( $l_{\text{eff}}$ )

for various inter-dome separation distances ( $s$ ) ranging from 5 to 35 nm with an interval of 5 nm when the background medium is air. It should be noted that, for fabricated devices, both inter-dome separation and cavity length decrease simultaneously as additional  $\text{SiO}_2$  is deposited onto the surface of the cylindrical polymer structure. Based on the results of experimentally measured  $\lambda_{\text{LSPR}}$  and inter-dome spacing ( $s$ ) from those points marked by the letters: I, J, and K shown in Figure 2(a), we identify the corresponding points: I', J' and K' with the approximately calculated effective cavity lengths of 78, 69 and 51 nm, as shown in the dashed curve of Figure 3.

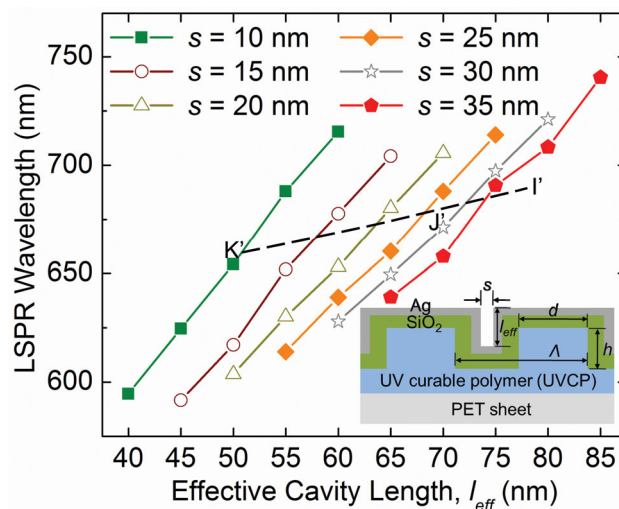


**Figure 3.** The FDTD-computed LSPR wavelength as a function of effective cavity length ( $l_{\text{eff}}$ ) for six different gap spacings ( $s$ ) for air as the background medium. The positions of the labeling of I', J' and K' were obtained by using experimental data shown in Figure 2 (a) enabling their respective effective cavity lengths can be calculated. The inset shows a FDTD-modeled Ag-PNA structure. This model is only valid for  $s > 0$ .



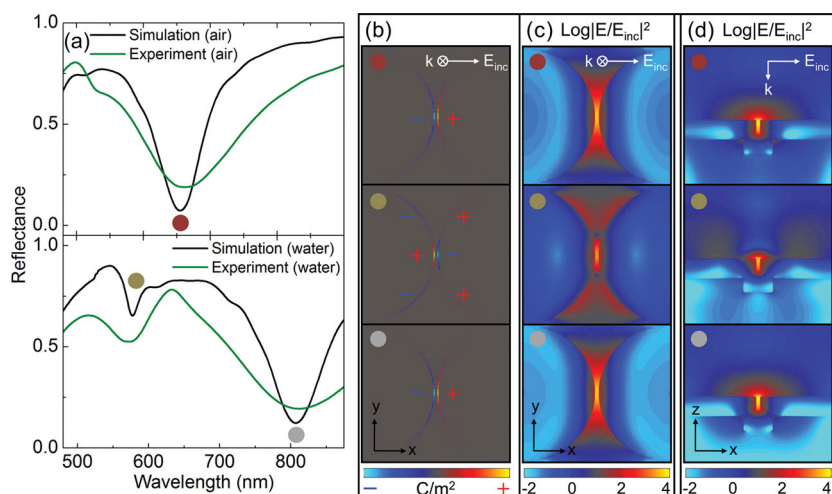


**Figure 4.** (a) Experimental and FDTD-computed reflection spectra of Ag-PNA substrate with  $s = 10$  nm for air and water as the background media. (b) Surface charge distributions associated with the corresponding resonances. The red and blue color represents the positive and negative charge, respectively. (c) Top and (d) cross-sectional electric-field intensity enhancement distributions associated with the indicated resonances.

Consequently, the blueshift of  $\lambda_{\text{LSPR}}$  can be attributed to the reduced effective nanocavity volume within the inter-dome space region as a consequence of additional SiO<sub>2</sub> coating. Moreover, since SERS enhancement is proportional to the product of the local electric-field intensity enhancement at the incident laser and the Raman scattered wavelength, the maximum  $|E|^2$  dependence on inter-dome spacing ( $s$ ) indicates that SERS intensity abruptly drops as the inter-dome separation distance ( $s$ ) increases (Supporting Information Figure S3).

The simulated reflectance spectra for the Ag-PNA structure with  $s = 10$  nm and  $l_{\text{eff}} = 51$  nm for the background media of air and water is presented by black curves in **Figure 4(a)**, which can be directly compared to the experimental data. The overall qualitative agreement between experimental and simulated profiles is excellent, and the remaining discrepancy of inhomogeneous linewidth broadening can be attributed to extra losses in the metal due to increased surface scattering, grain surface effects of the underlying SiO<sub>2</sub> film, and the inhomogeneity of the inter-dome separation. Surface charge distributions associated with the indicated plasmon resonances shown in **Figure 4(b)** illustrate that two lower-energy dipolar bonding modes centered around  $\lambda = 655$  nm in air and 807 nm in water, where the individual dipole moments of the nanodome are aligned and oscillate in phase, have an increased effective dipole moment, thus resulting in a broad continuum as well as higher resonant coupling efficiency in virtue of high radiative losses (scattering). The higher-energy hexapolar bonding mode occurs at  $\lambda = 577$  nm in water, where charges are partially canceled due to phase-retardation effects. This mode has a decreased effective dipole moment, resulting in linewidth narrowing as well as relatively lower resonant coupling efficiency as a result of significant reduction of radiative scattering of the PNA structure. **Figure 4(c)** and **(d)** respectively represent the electric-field intensity enhancement ( $\log|E/E_{\text{inc}}|^2$ ) distributions in the x-y and x-z

planes associated with the corresponding plasmon resonances. For the lower-energy broad modes resulting from strong dipolar couplings between adjacent nanodomains, the most intense field intensities are confined within the inter-dome space region, which is characteristic of the LSP modes. In contrast, for the higher-energy narrow mode arising from the suppression of radiative losses by hexapolar interactions, it is obvious that an evanescent electric field exists above the silver film, oriented in the  $z$  direction, which is characteristic for SPP modes (Supporting Information Figure S4). Moreover, the spectral location of the feature near  $\lambda = 571$  nm shown in the dotted curve of **Figure 2(b)** is almost invariant under varied inter-dome separation distances. Such variations only influence the excitation strength of the respective LSP modes as discussed earlier.

The coincidence between the experimentally measured and the numerically as well

as analytically calculated resonance positions (Supporting Information D) verifies that the observed resonance stems from the excitation of the (1,0) SPP mode via the periodic array of silver nanodomains.

## 2.2. Enhancement Characterization of Ag-PNA and Au-PNA Substrates

For experimental verification of SERS performance of the Ag-PNA substrates in air, a 5  $\mu\text{L}$  droplet of 1  $\mu\text{M}$  Rhodamine 6G (R6G, Sigma-Aldrich, 99%), a commonly used Raman analyte, was hand-spotted onto the Ag-PNA substrates, while a higher concentration (1 mM R6G) was applied to an ordinary glass slide coated with a 200 nm silver thin film for reference. Droplets were allowed to dry overnight before experiments were conducted. The diameter of one 5  $\mu\text{L}$  droplet of R6G is  $\sim 2.4$  mm and the spot size diameter of HeNe laser at an output power of 23  $\mu\text{W}$  is  $\sim 100$   $\mu\text{m}$ . Because the laser spot size is much smaller than the R6G droplet size and because the laser beam is focused near the center of the droplet where we observe uniform R6G concentration, we avoid measuring near the perimeter of the spot, where accumulation of crystalized material (the coffee ring effect) can occur. **Figure 5** shows SERS spectra of 1  $\mu\text{M}$  R6G on Ag-PNA substrates with four different inter-dome separation distances and 1 mM R6G on a silver reference sample using  $\lambda = 633$ -nm excitation. Although there are relative changes in amplitudes, all spectra show that the R6G molecule is characterized by seven dominant Raman peaks, centered at Raman shifts of 613, 771, 1184, 1312, 1363, 1512, and 1651  $\text{cm}^{-1}$ . We use the intensity at 1363  $\text{cm}^{-1}$ , the aromatic C–C stretching vibrational mode,<sup>[40]</sup> to quantitatively evaluate the analytical enhancement factor (AEF) of different Ag-PNA substrates (Supporting Information F). The enhancement of the 1363  $\text{cm}^{-1}$  Raman band strongly depends on the local electric field

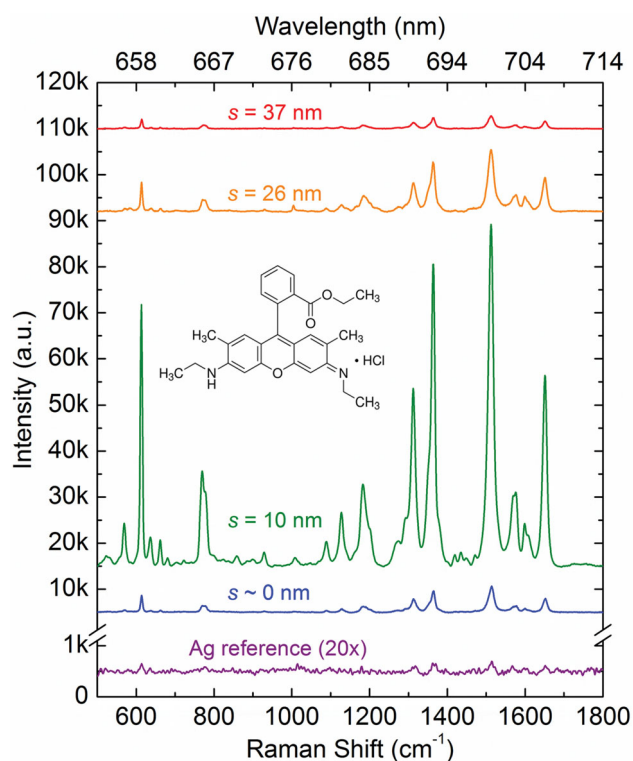


**Figure 5.** SERS spectra of 1  $\mu\text{M}$  R6G on different Ag-PNA substrates and 1 mM R6G on a silver reference sample (the reference spectrum was multiplied by a factor of 20 in the plot). All were excited by a  $\lambda = 633$  nm laser line.

intensity enhancement at the wavelengths of both the excitation and the  $1363\text{ cm}^{-1}$  shift, and it has been reported that the maximum EF occurs when  $\lambda_{\text{LSPR}}$  is located between  $\lambda_{\text{exc}}$  and  $\lambda_{\text{RS}}$  because LSPR is relatively broad and can be simultaneously excited by both incident the Raman scattered photons.<sup>[41]</sup> In addition to LSPR spectrally overlapping both  $\lambda_{\text{exc}}$  and  $\lambda_{\text{RS}}$ , R6G analytes spatially positioned within the hot spot region where the resonant electric-field intensity is greatest is also important because a small fraction of analytes under such an intense optical field can contribute a predominant portion of the overall SERS signal.<sup>[42]</sup> As shown in Figure 5 and Figure 2(a), when the inter-dome separation distances decrease from 37 to 10 nm, the SERS intensity gradually increases and  $\lambda_{\text{LSPR}}$  shifts from 690 to 660 nm, which lies halfway between  $\lambda_{\text{exc}}$  and  $\lambda_{\text{RS}}$ . In the case of  $s = 10$  nm, the AEF reaches the maximum value of  $9.43 \times 10^6$  because the maximum product of the local electric-field intensity enhancements at  $\lambda_{\text{exc}} = 632.8$  nm and  $\lambda_{\text{RS}} = 692.5$  nm occur within the 10-nm hot spot region. Afterward, the intensity abruptly drops down as adjoining nanodomains slightly touch each other due to the weaker electric field caused by few surface charges concentrating within the inter-dome spacing.

To more accurately quantify the SERS EF using a Raman-active probe molecule with a well-characterized surface density, and to avoid the effects of gradual degradation of Ag surfaces due to oxidation, we produced Au-PNA substrates. The Au surface allows reproducible growth of a self-assembled monolayer of trans-1,2-bis(4-pyridyl)ethylene (BPE,

Sigma-Aldrich, 97%) because BPE molecules are able to interact with gold via the pyridyl nitrogen atoms.<sup>[43]</sup> The use of an Au-PNA surface also allows direct performance comparison to a commercially available SERS substrate (Klarite KLA-313, D3 Technologies Ltd., UK) that is comprised of Au-coated etched pyramids on a silicon substrate. Au-PNA fabrication follows the same procedure as Ag-PNA fabrication, with the substitution of a 160-nm-thick gold film for the previous silver film. Although freshly produced silver-based nanostructures generally provide higher EF than gold-based devices,<sup>[28]</sup> gold is more compatible with our target applications for detection of drugs and metabolites in fluid. Before measurements were conducted, an Au-PNA substrate with  $s = 10$  nm and a Klarite substrate were immersed in 10  $\mu\text{M}$  BPE ethanolic solution for 12 h and then rinsed in pure ethanol, followed by blow drying with nitrogen to ensure a uniform single molecular layer adsorbed on the surfaces.<sup>[43,44]</sup> A neat 100 mM BPE ethanolic solution poured into a cell culture dish (Corning 430166) with the dimensions of  $60 \times 15$  mm for diameter and height was used as the reference.

**Figure 6(a)** shows the SERS spectra of surface-adsorbed BPE on Au-PNA with  $s = 10$  nm and Klarite substrates and the Raman spectrum of 100 mM aqueous BPE solution using  $\lambda = 633$ -nm excitation. All spectra show the five characteristic peaks of BPE at 1000/1020, 1200, 1340, 1607, and  $1637\text{ cm}^{-1}$ . The integrated intensity of the band at  $1200\text{ cm}^{-1}$ , the C = C stretching vibrational mode,<sup>[45]</sup> was selected to quantitatively assess performance for each substrates and determine the spatially averaged SERS EF of the Au-PNA substrate. It is obvious that SERS intensities are substantially greater when BPE molecules are adsorbed onto the SERS-active surface of the Au-PNA substrate compared to that of the Klarite substrate. The integrated intensity of the band at  $1200\text{ cm}^{-1}$  normalized by the laser power and CCD integration time obtained from Au-PNA substrate outperforms that from the Klarite SERS substrate by 238x. As shown in Figure 6(b), the lower SERS signal of the Klarite substrate can be attributed to the LSPR wavelength of this surface (measured  $\lambda_{\text{LSPR}}$  of 735 nm) which is located far beyond the excitation wavelength and Raman scattered wavelength ( $\lambda_{\text{RS}} = 684.8$  nm), corresponding to the evaluated Raman shift of  $1200\text{ cm}^{-1}$ . For the SERS spectrum of surface-adsorbed BPE on the Klarite substrate excited by a 785 nm laser line please refer to Supporting Information Figure S5 for more information. After subtracting the background of the raw SERS and Raman spectra using a sixth-order polynomial fit, the calculation of the spatially averaged SERS EF is based on the equation:  $\text{EF} = [I_{\text{SERS}}(\lambda_{\text{Raman}})/N_{\text{SERS}}]/[I_{\text{Ref}}(\lambda_{\text{Raman}})/N_{\text{Ref}}]$ .<sup>[46]</sup>  $I_{\text{SERS}}(\lambda_{\text{Raman}})$  and  $I_{\text{Ref}}(\lambda_{\text{Raman}})$  are the integrated intensity of the band at  $\lambda_{\text{Raman}} = 1200\text{ cm}^{-1}$  normalized by the laser power and CCD integration time from the SERS spectrum of surface-adsorbed BPE on Au-PNA substrate and Raman spectrum of bulk liquid BPE, respectively.  $N_{\text{SERS}}$  and  $N_{\text{Ref}}$  are the number of excited BPE molecules inside the laser spot area on the Au-PNA surface and within the laser probe volume in 100 mM BPE solution, contributing to measured SERS and Raman intensities, respectively.  $N_{\text{SERS}}$  was calculated using  $N_{\text{SERS}} = \rho SA/p2$ , where  $\rho$  is the surface density of BPE molecules, which is estimated to be  $3.3 \times 10^{14}\text{ cm}^{-2}$  based

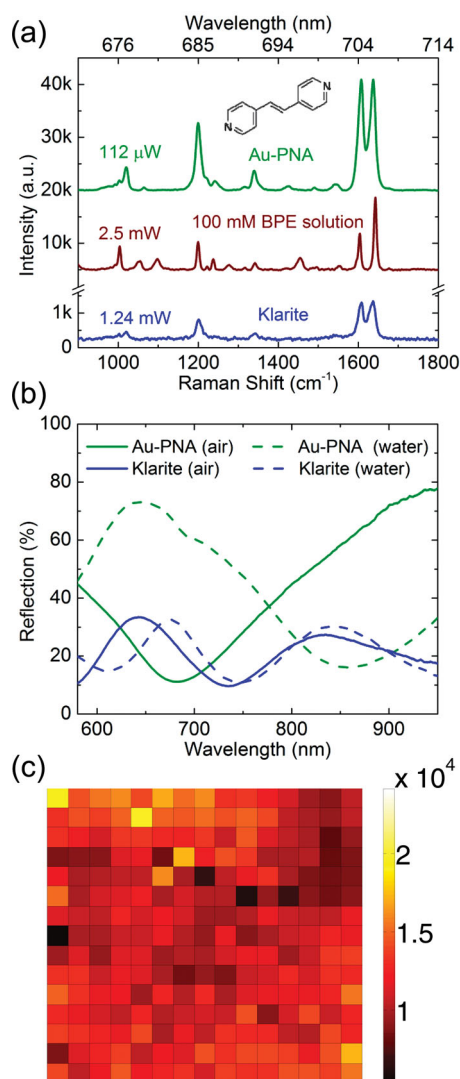


**Figure 6.** (a) SERS spectrum of surface-adsorbed BPE on Au-PNA with 10-nm gap spacing, SERS spectrum from a Klarite substrate, and the Raman spectrum of 100 mM aqueous BPE solution. All were excited by a  $\lambda = 633$  nm laser line with the output power values showing in the figure. (b) Measured far-field reflection spectra of Au-PNA and Klarite substrates, showing their respective  $\lambda_{\text{LSPR}}$  of 681 and 735 nm in air and 858 and 609/747 nm in water. (c) SERS intensity distribution map measured at  $1200 \text{ cm}^{-1}$  for the Au-PNA substrate with  $s = 10$  nm over an area of  $9 \text{ mm}^2$ .

on a  $30 \text{ \AA}^2$  approximate area of a single BPE molecule,<sup>[44]</sup>  $S$  is the total surface area of a unit cell of the Au-PNA, which includes the top plateau and the side wall surfaces as well as the base surface,  $A$  is the laser spot area, and  $p$  is the period of the PNA structure.  $N_{\text{Ref}}$  was calculated using  $N_{\text{Ref}} = c N_A V$ , where  $c$  is the molar concentration of bulk BPE solution,  $N_A$  is Avogadro's number, and  $V$  is the laser probe volume. The laser probe volume is assumed to be that of a cylinder with a diameter and a height equivalent to the measured laser spot size and the effective probe length.<sup>[28,47]</sup> The effective probe length was determined by immersing a silicon substrate into a neat ethanol solution in a cell culture dish (Corning 430166) while recording the background-subtracted

silicon Raman peak at  $522 \text{ cm}^{-1}$  at each  $z$  position when the stage was translated vertically. Using a 5 $\times$  objective ( $\text{NA} = 0.12$ ) with an output laser power of 2.5 mW, the effective probe length was measured to be 9 nm. Hence the spatially averaged SERS EF is calculated to be  $8.51 \times 10^7$ . Figure 6(c) presents a spatial map of SERS intensities at  $1200 \text{ cm}^{-1}$  on the Au-PNA substrate with 10-nm gap spacing and this map also shows that more than 78.5% coverage has spatially averaged SERS EFs above  $6.68 \times 10^7$ , demonstrating the excellent uniformity of high EFs over an area of  $9 \text{ mm}^2$ .

### 2.3. SERS Detection of Urea

For experimental demonstration of SERS performance of the Au-PNA substrate in an aqueous solution, a flow cell with inlet/outlet at the ends for outside tubing connection made of an optically clear resin (WaterClear Ultra 10122, DSM Somos) was first sandwiched between a cover glass and the Au-PNA substrate with  $s = 10$  nm using UV-cured adhesive (Addison Clear Wave). Urea solution prepared at concentrations of 12.5, 25, 50, 100, 150, and 200 mM in DI water was then manually pumped into the flow cell using a syringe. Each concentration measurement was taken five times at the same location without flow, followed by emptying and rinsing with DI water three times before beginning the next concentration measurement. **Figure 7** shows SERS spectra of urea solutions and DI water (blank) on the Au-PNA substrate with  $s = 10$  nm using  $\lambda = 785$ -nm excitation. We used a 5 $\times$  low-NA objective ( $\text{NA} = 0.12$ ) with a long working distance of 14 mm in a Renishaw inVia Raman microscope. It is obvious that the SERS spectra for urea solution exhibits a primary Raman

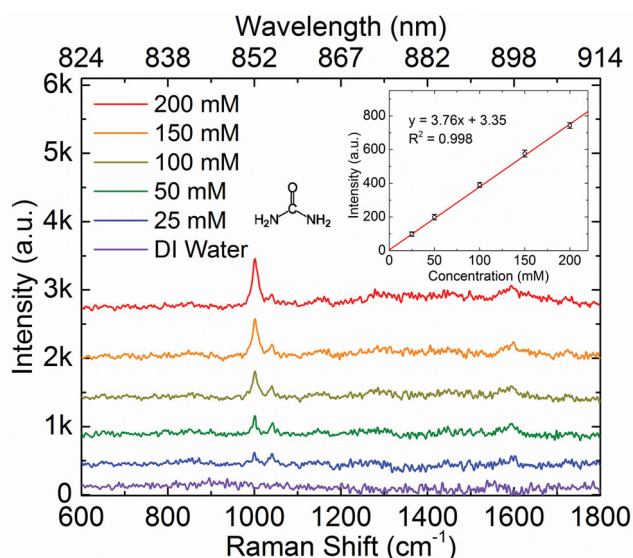


**Figure 7.** SERS spectra of urea solutions and DI water as the blank for Au-PNA substrate with  $s = 10$  nm attached to a flow cell. All were excited by  $\lambda = 785$  nm laser line with the output laser power of 7.8 mW delivered to the sample. Primary intensity peak for urea can be observed at  $1000 \text{ cm}^{-1}$ . The inset represents averaged SERS intensity measured at  $1000 \text{ cm}^{-1}$  as a function of urea concentration with error bars indicating  $\pm 1$  standard deviation ( $N = 5$ ).



band at  $1000\text{ cm}^{-1}$ , the symmetrical C–N stretching vibrational mode.<sup>[48]</sup> The inset presents a calibration curve of the averaged SERS intensity at  $1000\text{ cm}^{-1}$  as a function of urea concentration with error bar representing  $\pm 1$  standard deviation ( $\sigma$ ) of five measurements at the same location. The data points were linearly fit by a least squares approximation with an  $R^2$  value of 0.998. The limit of detection (LOD) is defined as the concentration at which the intensity value is equal to the averaged blank intensity at  $1000\text{ cm}^{-1}$  plus three times the standard deviation of five blank intensities at  $1000\text{ cm}^{-1}$ . Using the calibration curve to convert this intensity value to the corresponding concentration, i.e., LOD, the LOD for urea solutions was calculated to be 11.9 mM for the Au-PNA substrate. Compared to LOD of 3.93 mM obtained from the Ag-PNA substrate (Supporting Information Figure S6) with an LSPR wavelength of 811 nm shown in Figure 2(b), the higher LOD of 11.9 mM can be attributed to the fact that the LSPR wavelength of 858 nm shown in Figure 6(b) is not within the spectral region between the excitation wavelength and Raman scattered wavelength ( $\lambda_{\text{RS}} = 852\text{ nm}$ ), corresponding to the designated Raman shift of  $1000\text{ cm}^{-1}$ . We envision application of this approach to detection of metabolites within biomedical tubing used for urinary catheters or renal dialysis, as a means for continuous monitoring of kidney function. Our detection approach is based upon diffusion of the analyte into the SERS-active volume without the need for surface adsorption, making this method suitable for in-line real-time monitoring, where accumulation of material onto the PNA surface by a selective capture coating is not desired. The LOD reported may be improved through the use of a high-NA objective to collect more scattered Raman photons, but at the expense of a working distance that would not be compatible with our flow cell, which must be deep enough to accommodate substantial flow rates. (See Supporting Information I and J for further details). The obtained LOD of 11.9 mM is sufficient for our clinical applications, as this value is well below the typical level of urea concentration in urine,  $273\text{ mM}$ <sup>[48]</sup> and the pathophysiological range of urea concentration in blood,  $30\text{--}150\text{ mM}$ ,<sup>[49]</sup> suggesting that our PNA substrate can provide a rapid and quantitative testing method for the detection of kidney activity and urine screening.

### 3. Conclusion

We have successfully demonstrated that a PNA substrate can be fabricated using a low-cost, large-area and high-throughput nanoreplica molding technique, which provides a high density of EM hot spots. The spatially averaged SERS EF was measured to be  $8.51 \times 10^7$  when the LSPR is spectrally located between the excitation and Raman scattered wavelengths. Mapping of the SERS EF demonstrates that spatially averaged EFs higher than  $6.68 \times 10^7$  remains consistent over a large SERS-active surface. As an exemplary clinical application of the sensor for detection of a urinary metabolite, urea in solution was detected with a detection limit of 11.9 mM, indicating the potential for in-line, real-time monitoring for detection of fluid samples from patients without taking samples and performing laboratory based tests.

### 4. Experimental Section

**Nanostructure Fabrication:** To produce a template used for the molding, nanoimprint lithography (Molecular Imprints) and reactive ion etching were used to pattern an 8-inch diameter silicon wafer with a 2-dimensional array of 250 nm diameter holes (period = 400 nm, depth = 130 nm), in  $8 \times 8\text{ mm}^2$  dies with overall feature dimensions of  $96 \times 64\text{ mm}^2$ . Next, a negative volume image of the silicon surface structure was formed by dispensing liquid UV curable polymer (Gelest) droplets (total volume of  $\sim 500\text{ }\mu\text{L}$ ) and distributing between the silicon wafer and a 200  $\mu\text{m}$  thick flexible polyethylene terephthalate (PET) sheet using a roller. Based on the polymer dispense volume and the distributed area, the spacing between the silicon wafer and the PET sheet is  $\sim 10\text{ }\mu\text{m}$ . After curing by exposure to UV light, the molded structure was released from the wafer by peeling away the PET, resulting in a polymer replica of the silicon wafer structure adhering to the PET sheet. To minimize the separation distance between adjacent polymer cylinders, i.e.  $\Delta d$ , we control the thickness of the  $\text{SiO}_2$  film (applied by sputter deposition) which conformally coats the surface of cylinders, where their diameter increases with increasing  $\text{SiO}_2$  thickness. To complete the fabrication, the PNA surface was blanketed with a 10 nm Ti adhesion layer and then a 200-nm-thick Ag or a 160-nm-thick Au film in an electron beam evaporation system (Temescal).

**Reflection Measurements:** In order to understand the LSPR wavelength dependence on inter-dome spacing ( $s$ ), far field reflection measurements of the PNA substrates deposited with varied  $\text{SiO}_2$  thicknesses were carried out using an Axio Observer D1 inverted microscope (Carl Zeiss, Inc.) with white light provided by a halogen lamp and a  $10\times$  objective (NA = 0.25) connected to a VIS-NIR spectrometer (Control Development, Inc.) through an optical fiber. For reflection measurements of PNA substrates immersed with water covering the surface, a water droplet ( $10\text{ }\mu\text{L}$ ) was hand-spotted onto the nanodome surface, and covered with a microscope cover glass prior to measurement. All reflection spectra were collected against a 200-nm-thick mirror-like Ag film over microscope glass slide as the reference. For reflection measurements of Klarite and Au-coated PNA substrates, a 200-nm-thick Au film deposited upon a glass slide was used as the reference.

**Modeling:** A commercial software package (FDTD Solutions, Lumerical Solutions Inc.) was used to simulate the optical responses of Ag-PNA structures. The structure was excited by a normally incident, unit magnitude plane wave propagating in the  $-z$  direction with an electric field polarization along the  $x$ -axis. In order to decrease the computation time, periodic anti-symmetric and symmetric boundary conditions were imposed at  $x$  and  $y$  boundaries of the  $x$ - $y$  plane, respectively. Perfectly matched layers are imposed at boundaries of the propagation direction to properly absorb incident radiation. Monitors were placed to calculate the amount of reflected, transmitted, absorbed power as a function of wavelength. The optical properties of Ag and  $\text{SiO}_2$  were taken from Palik's handbook.<sup>[50]</sup>

**Raman Measurements:** Raman measurements were carried out by using a Renishaw inVia Raman microscope equipped with a 8 mW HeNe laser ( $\lambda_{\text{exc}} = 632.8\text{ nm}$ ), a 200 mW NIR diode laser ( $\lambda_{\text{exc}} = 785\text{ nm}$ ), and a  $5\times$  objective (NA = 0.12) with a working distance of 14 mm. The measured HeNe laser power at the exit of the objective is respectively 23 and 112  $\mu\text{W}$  on measurements of R6G on Ag-PNA and BPE on Au-PNA substrates, and the measured NIR

diode laser power at the exit of the objective is respectively 7.8 and 30.2 mW on urea detection on Au-PNA and Ag-PNA substrates. The laser power of 1.24 mW was delivered to the Klarite substrate for both the HeNe and the NIR diode lasers. The scattered photons were collected by the same objective lens and sent through a holographic notch filter and a Peltier-cooled CCD detector to acquire SERS spectra. All experimental data were gathered using a linearly polarized laser beam orientated in the x-axis with an integration time of 10 s.

## Supporting Information

Supporting Information is available from the Wiley Online Library or from the author.

## Acknowledgements

The authors thank the staff of the Micro and Nanotechnology Laboratory and the Center for Nanoscale Chemical–Electrical–Mechanical Manufacturing Systems (Nano-CEMMS) at the University of Illinois at Urbana-Champaign. This work was supported by the National Science Foundation under Award No. CBET 07-54122 and ECCS 09-24062. Any opinions, findings, and conclusions or recommendations expressed in this material are those of the author(s) and do not necessarily reflect the views of the National Science Foundation. The authors declare no competing financial interests.

- [1] P. P. Pompa, L. Martiradonna, A. D. Torre, F. D. Sala, L. Manna, M. De Vittorio, F. Calabi, R. Cingolani, R. Rinaldi, *Nat. Nanotechnol.* **2006**, *1*, 126.
- [2] K. Aslan, M. Wu, J. R. Lakowicz, C. D. Gedde, *J. Am. Chem. Soc.* **2007**, *129*, 1524.
- [3] K. Nakatani, S. Sando, I. Saito, *Nat. Biotechnol.* **2001**, *19*, 51.
- [4] K. A. Willets, R. P. Van Duyne, *Annu. Rev. Phys. Chem.* **2007**, *58*, 267.
- [5] S. Lal, S. Link, N. J. Halas, *Nat. Photonics* **2007**, *1*, 641.
- [6] D.-K. Lim, K.-S. Jeon, J.-H. Hwang, H. Kim, S. Kwon, Y. D. Suh, J.-M. Nam, *Nat. Nanotechnol.* **2011**, *6*, 452.
- [7] M. L. Juan, M. Righini, R. Quidant, *Nat. Photonics* **2011**, *5*, 349.
- [8] K. Wang, E. Schonbrun, P. Steinvurzel, K. B. Crozier, *Nat. Commun.* **2011**, *2*, 469.
- [9] R. F. Oulton, V. J. Sorger, T. Zentgraf, R.-M. Ma, C. Gladden, L. Dai, G. Bartal, X. Zhang, *Nature* **2009**, *461*, 629.
- [10] R.-M. Ma, R. F. Oulton, V. J. Sorger, G. Bartal, X. Zhang, *Nat. Mater.* **2011**, *10*, 110.
- [11] K. R. Catchpole, A. Polman, *Optics Express* **2008**, *16*, 21793.
- [12] H. A. Atwater, A. Polman, *Nat. Mater.* **2010**, *9*, 205.
- [13] P. L. Stiles, J. A. Dieringer, N. C. Shah, R. P. Van Duyne, *Annu. Rev. Anal. Chem.* **2008**, *1*, 601.
- [14] J. N. Anker, W. P. Hall, O. Lyandres, N. C. Shah, J. Zhao, R. P. Van Duyne, *Nat. Mater.* **2008**, *7*, 442.
- [15] S. Nie, S. R. Emory, *Science* **1997**, *275*, 1102.
- [16] K. Kneipp, Y. Wang, H. Kneipp, L. T. Perelman, I. Itzkan, R. R. Dasari, M. S. Feld, *Phys. Rev. Lett.* **1997**, *78*, 1667.
- [17] R. G. Freeman, K. C. Grabar, K. J. Allison, R. M. Bright, J. A. Davis, A. P. Guthrie, M. B. Hommer, M. A. Jackson, P. C. Smith, D. G. Walter, M. J. Natan, *Science* **1995**, *267*, 1629.
- [18] S. B. Chaney, S. Shanmukh, R. A. Dluhy, Y. P. Zhao, *Appl. Phys. Lett.* **2005**, *87*, 031908.
- [19] X. M. Qian, S. M. Nie, *Chem. Soc. Rev.* **2008**, *37*, 912.
- [20] D. He, H. Bo, Q.-F. Yao, K. Wang, S.-H. Yu, *ACS Nano* **2009**, *3*, 3993.
- [21] J. Theiss, P. Pavaskar, P. M. Echternach, R. E. Muller, S. B. Cronin, *Nano Lett.* **2010**, *10*, 2749.
- [22] H.-Y. Wu, B. T. Cunningham, *Appl. Phys. Lett.* **2011**, *98*, 153103.
- [23] J. J. Mock, R. T. Hill, A. Degiron, S. Zauscher, A. Chilkoti, D. R. Smith, *Nano Lett.* **2008**, *8*, 2245.
- [24] C. L. Haynes, R. P. Van Duyne, *J. Phys. Chem. B* **2001**, *105*, 5599.
- [25] L. A. Dick, A. D. McFarland, C. L. Haynes, R. P. Van Duyne, *J. Phys. Chem. B* **2002**, *106*, 853.
- [26] Q. Yu, P. Guan, D. Qin, G. Golden, P. M. Wallace, *Nano Lett.* **2008**, *8*, 1923.
- [27] J. Petschulat, D. Cialla, N. Janunts, C. Rockstuhl, U. Hubner, R. Moller, H. Schneidewind, R. Mattheis, J. Popp, A. Tunnermann, F. Lederer, T. Pertsch, *Optics Express* **2010**, *18*, 4184.
- [28] Y. Chu, M. G. Banaee, K. B. Crozier, *ACS Nano* **2010**, *4*, 2804.
- [29] H. Im, K. C. Bantz, N. C. Lindquist, C. L. Haynes, S.-H. Oh, *Nano Lett.* **2010**, *10*, 2231.
- [30] A. W. Clark, A. Glidle, D. R. S. Cumming, J. M. Cooper, *J. Am. Chem. Soc.* **2009**, *131*, 17615.
- [31] A. W. Clark, J. M. Cooper, *Adv. Mater.* **2010**, *22*, 4025.
- [32] A. W. Clark, J. M. Cooper, *Small* **2011**, *7*, 119.
- [33] C. J. Choi, Z. Xu, H.-Y. Wu, G. L. Liu, B. T. Cunningham, *Nanotechnology* **2010**, *21*, 415301.
- [34] J. D. Caldwell, O. Glembocki, F. J. Bezares, N. D. Bassim, R. W. Rendell, M. Feygelson, M. Ukaegbu, R. Kasica, L. Shirey, C. Hosten, *ACS Nano* **2011**, *5*, 4046.
- [35] J. D. Caldwell, O. J. Glembocki, F. J. Bezares, M. I. Kariniemi, J. T. Niinistö, T. T. Hatanpää, R. W. Rendell, M. Ukaegbu, M. K. Ritala, S. M. Prokes, C. M. Hosten, M. A. Leskelä, R. Kasica, *Optics Express* **2011**, *19*, 26056.
- [36] C.-F. Chen, S.-D. Tzeng, H.-Y. Chen, K.-J. Lin, S. Gwo, *J. Am. Chem. Soc.* **2008**, *130*, 824.
- [37] J. P. Kottmann, O. J. F. Martin, *Optics Express* **2001**, *8*, 655.
- [38] W. Rechberger, *Optics Commun.* **2003**, *220*, 137.
- [39] M. Bora, B. J. Fassenfest, E. M. Behymer, A. S. P. Chang, H. T. Nguyen, J. A. Britten, C. C. Larson, J. W. Chan, R. R. Miles, T. C. Bond, *Nano Lett.* **2010**, *10*, 2832.
- [40] N. Hayazawa, Y. Inouye, Z. Sekkat, S. Kawata, *J. Chem. Phys.* **2002**, *117*, 1296.
- [41] C. L. Haynes, C. R. Yonzon, X. Zhang, R. P. Van Duyne, *J. Raman Spectrosc.* **2005**, *36*, 471.
- [42] Y. Fang, N.-H. Seong, D. D. Dlott, *Science* **2008**, *321*, 388.
- [43] A. Kim, F. S. Ou, D. A. A. Ohlberg, M. Hu, R. S. Williams, Z. Li, *J. Am. Chem. Soc.* **2011**, *133*, 8234.
- [44] N. Féridj, J. Aubard, G. Lévi, J. R. Krenn, M. Salerno, G. Schider, B. Lamprecht, A. Leitner, F. R. Aussenegg, *Phys. Rev. B* **2002**, *65*, 075419.
- [45] H. Y. Chu, Y. Liu, Y. Huang, Y. Zhao, *Optics Express* **2007**, *15*, 12230.
- [46] E. C. Le Ru, E. Blackie, M. Meyer, P. G. Etchegoin, *J. Phys. Chem. C* **2007**, *111*, 13794.
- [47] Y. S. Hu, J. Jeon, T. J. Seok, S. Lee, J. H. Hafner, R. A. Drezek, H. Choo, *ACS Nano* **2010**, *4*, 5721.
- [48] W. R. Premasiri, R. H. Clarke, M. E. Womble, *Lasers in Surgery and Medicine* **2001**, *28*, 330.
- [49] D. G. Pijanowska, M. Dawgul, W. Torbicz, *Sensors* **2003**, *3*, 160.
- [50] E. D. Palik, *Handbook of Optical Constants of Solids*, Academic Press, Orlando, FL **1985**.

Received: April 2, 2012  
Published online: